

# Experimental Characterization and Quadratic Programming-Based Control of Brushless-Motors

Farhad Aghili, Martin Buehler, and John M. Hollerbach

**Abstract**—A new torque control strategy for brushless motors is presented, which results in minimum torque ripple and copper losses. The motor model assumes linear magnetics, but contains a current limit which can delimit the onset of magnetic saturation, or be the motor amplifier current limit, whichever is reached first. The control problem is formulated and solved as a quadratic programming problem with equality and inequality constraints to find the nonlinear mapping from desired torque and position to the motor's phase currents. The optimal solution is found in closed form using the Kuhn–Tucker theorem. The solution shows that, unlike the conventional commutation with a fixed current-position waveform, the waveforms of the proposed controller vary in order to respect the current limitation in one phase by boosting the current in the other phases. This increases the maximum torque capability of the motor—in our particular system by 20%—compared to fixed waveform commutation. Experimental data from our brushless direct-drive motor demonstrates that the controller produces virtually ripple-free torque and enhances remarkably the tracking accuracy of the motion controller.

**Index Terms**—Brushless motor, motor control, optimal control, quadratic programming, torque control.

## I. INTRODUCTION

**P**RECISE position tracking is critical in many robotic and automation applications such as arc welding, laser cutting, NC machining, fixture-less assembly, or precise indexing. Direct-drive brushless motors are ideal candidates for such applications. They can, in principle, substantially improve the positioning precision since they lack the gears required in conventional electric drive systems. However, by the same token, direct-drive systems are more adversely affected by the motor's torque ripple. Moreover, direct-drive motors suffer from relatively low torque capability, limited by power losses and current saturation. Ideally, a controller must solve three tasks simultaneously: Minimize torque ripple, minimize copper losses, and maximize the torque capability with respect to current limitation. This paper presents such a controller.

Direct-drive motors are multidimensional nonlinear systems composed of both mechanical and electrical subsystems. In the realm of control of electromechanical systems, phase voltage and joint angle or velocity are often considered as the system input and output leading to complicated nonlinear input–output

Manuscript received March 14, 2001; revised February 7, 2002. Manuscript received in final form July 8, 2002. Recommended by Associate Editor S. Bortoff. This work was supported in part by MPB Technologies, Montréal, QC, Canada, under the PRECARN TDS Project.

F. Aghili is with the Canadian Space Agency, Space Technologies, Spacecraft Engineering, Saint-Hubert, QC H3A 2A7, Canada (e-mail: farhad.aghili@space.gc.ca).

M. Buehler is with the Department of Mechanical Engineering, McGill University, Montreal, QC J3Y 8Y9, Canada (e-mail: buehler@cim.mcgill.ca).

J. M. Hollerbach is with the School of Computing, University of Utah, Salt Lake City, UT 84112 USA (e-mail: jmh@cs.utah.edu).

Digital Object Identifier 10.1109/TCST.2002.806453

dynamics. Control strategies based on feedback linearization [9], [16], [18], singular perturbation [14], [17], and adaptive schemes [14] have been proposed in the past. Shouse *et al.* [14], [15] presented a digital self-tuning controller for permanent-magnet synchronous motors, providing for either velocity or position tracking. Taylor [17] applied a digital reduced-order modeling to velocity control design for permanent-magnet synchronous motors minimizing copper losses.

The control problem is radically simplified when the motor's phase currents are considered as the inputs as opposed to the armature voltages. Then the control problem is reduced to the torque control of motors, which is a nonlinear mapping from desired torques and positions to phase currents, and the control of the multibody dynamics of the manipulator that traditionally relies on torque control inputs. Control approaches for accurate torque production in direct-drive systems and their underlying models have been studied by several researchers [5], [12], [16], [19]. Murai *et al.* [13] proposed a heuristic commutation scheme for nonsinusoidal flux distribution. Le-Huy *et al.* [4], [11] reduced the torque ripple harmonics for brushless dc motors by using several drive current waveforms. Ha and Kang [6] completely characterized in an explicit form the class of feedback controllers that produce ripple-free torque in brushless motors. A free function can be used to achieve other control objective, such as minimization of power dissipation, but phase current saturation was not considered. Optimal torque control, but without taking current limitation into account, was addressed in [3] and [8].

The main contribution of this paper is the design of a ripple-free torque controller that minimizes copper losses and maximizes the torque capability of the motor under current limitation. In conventional commutation approaches with fixed current–angle waveforms, the maximum torque is reached when at least one phase current saturates. In our scheme, through the application of constrained optimization, the waveforms vary to compensate saturated (current limited) phases by boosting currents of the unsaturated phases. This tends to increase the maximum torque capability of the motor while operating in a linear magnetic regime. In this scheme, the motor torque capability is increased because the motor can produce more torque until the currents of all phases saturate. Furthermore, contrary to the past approaches, the proposed strategy does not rely on any condition for the phase torque–angle waveforms, e.g., having balanced phases which imposes the KCL constraint at the floating neutral node. An experimental motor characterization and a real-time controller implementation on a hydraulic dynamometer test-bed documents the validity of our claims.

Section II presents the optimal torque control of general multiphase brushless motors, based on quadratic programming with equality and inequality constraints. The optimal solution

is derived via the Kuhn–Tucker theorem [10]. Section III shows analytically that by considering current saturation, the maximum motor torque is increased. In Section IV, the experimental hydraulic dynamometer testbed is described, and the phase torque–angle and torque–current characteristics are identified experimentally for the McGill/MIT motor [2], [7], a synchronous direct-drive motor with axial air gap. The performance of the proposed commutation to produce virtually ripple-free torque, to yield precise position tracking, and to increase the motor’s torque capability is demonstrated experimentally in Section V.

## II. OPTIMAL PHASE CURRENT

### A. Motor Model

We assume that there is negligible cross-coupling between the phase torques and there is no reluctance torque. In addition, we assume that the phase currents can be controlled accurately and instantaneously so that the phase currents can be treated as the control inputs. Then, the torque developed by a single phase is a function of the phase current  $x_j$  and the (angular motor) position  $\theta$

$$\tau_j(x_j, \theta) = x_j a_j(\theta), \quad j \in \mathcal{J} = \{1, 2, \dots, n\} \quad (1)$$

where  $a_j(\theta)$  is the position nonlinearity associated with the  $j$ th phase, or torque shape function. For brevity, we shall omit the argument  $\theta$  in the sequel. The motor torque  $\tau$  is the superposition of all phase torque contributions

$$\tau = \sum_{j=1}^n x_j(\theta, \tau_d) a_j. \quad (2)$$

The torque control problem is to solve the above equation in terms of current,  $x_j(\theta, \tau_d)$ , as a function of motor position, given a desired motor torque  $\tau_d$ . Given a scalar torque set point, (2) permits infinitely many (position-dependent) phase current wave forms. Since the continuous mechanical power output of electrical motors is limited primarily by heat generated from internal copper losses, it makes sense to use the freedom in the phase current solutions to minimize power losses

$$P_{loss} = R \sum_{j=1}^n x_j^2(\theta, \tau_d) \quad (3)$$

where  $R$  is the armature resistance. Current saturation is the other limitation which should be considered. Let  $x_{\max} > 0$  be the maximum equivalent phase current corresponding to a linear phase current–torque relationship, i.e., (1) is valid, or to current limit of the servoamplifier. Then, the phase currents must satisfy

$$|x_j| \leq x_{\max}, \quad \forall j \in \mathcal{J}. \quad (4)$$

### B. Quadratic Programming

In order to derive the optimal phase currents  $x_j^*(\theta, \tau_d)$  which generate the desired torque (2) and minimize the power losses

(3) subject to the constraints (4) we need the torque functions  $a_j(\theta)$ . Let the functions be represented in a discrete manner at a finite number of motor positions. Then, the values of the functions at any specific position  $\theta$ , i.e.,  $\{a_1(\theta), \dots, a_n(\theta)\}$ , can be interpolated. Hereafter, we drop the argument  $\theta$  for simplicity. Now, by setting  $\tau = \tau_d$  in (2), the problem of finding optimal phase currents that minimize power losses subject to the constraints is formulated by the quadratic programming problem

$$\min f(\mathbf{x}) = x_1^2 + x_2^2 + \dots + x_n^2 \quad (5)$$

$$h(\mathbf{x}) = a_1 x_1 + a_2 x_2 + \dots + a_n x_n - \tau_d = 0 \quad (6)$$

$$g_j(\mathbf{x}) = |x_j| - x_{\max} \leq 0, \quad j \in \mathcal{J} \quad (7)$$

where  $\mathbf{x} = [x_1, x_2, \dots, x_n]^T \in \mathfrak{R}^n$  is the vector of design variables. Since all the functions are convex, any local minimum is a global minimum as well. Now, we seek the minimum point  $\mathbf{x}^* = [x_1^*, x_2^*, \dots, x_n^*]^T$  satisfying the equality and inequality constraints. Before we pay attention to the general solution, it is beneficial to exclude the trivial solution,  $x_j^* = 0$ . If the  $j$ th torque shape function is zero, that phase contributes no torque regardless of its current. Hence

$$a_j = 0 \implies x_j^* = 0 \quad \forall j \in \mathcal{J} \quad (8)$$

immediately specifies the optimal phase currents at the crossing point. By excluding the trivial solution, we deal with a smaller set of variables and number of equations in our optimization programming. Therefore, we have to find the optimal solution corresponding to the nonzero part. Hereafter, without loss of generality, we assume that all torque shape functions are nonzero.

Now, by defining the function

$$\mathcal{L}(\mathbf{x}) = f(\mathbf{x}) + \lambda h(\mathbf{x}) + \boldsymbol{\mu}^T \mathbf{g}(\mathbf{x}) \quad (9)$$

the optimal point can be found by using the Kuhn–Tucker theorem.

*Theorem 1 [10]:* Let  $\mathbf{x}^*$  provide a local minimum of  $f(\mathbf{x})$  satisfy the equality and inequality constraints  $h(\mathbf{x}) \in \mathfrak{R}$ , and  $\mathbf{g}(\mathbf{x}) = [g_1(\mathbf{x}), g_2(\mathbf{x}), \dots, g_n(\mathbf{x})]^T \in \mathfrak{R}^n$ . Assuming that vectors  $(\partial g_j / \partial \mathbf{x})^T|_{\mathbf{x}=\mathbf{x}^*}$ , ( $j \in \mathcal{J}$ ) are linearly independent, then there exist  $\lambda \in \mathfrak{R}$  and  $\boldsymbol{\mu} = [\mu_1, \mu_2, \dots, \mu_n]^T \geq 0 \in \mathfrak{R}^n$  such that

$$\nabla_{\mathbf{x}} \mathcal{L}(\mathbf{x}^*) = 0 \quad (10)$$

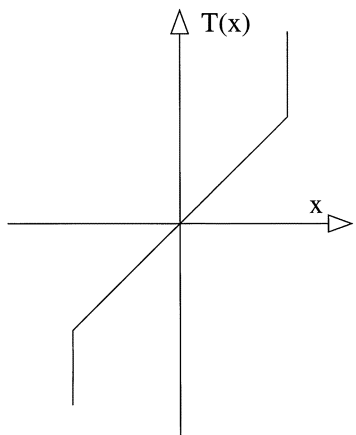
$$\nabla_{\lambda} \mathcal{L}(\mathbf{x}^*) = 0 \quad (11)$$

$$\boldsymbol{\mu}^T \mathbf{g}(\mathbf{x}^*) = 0. \quad (12)$$

Let  $\text{sgn}(\cdot)$  represents the sign function, where

$$\text{sgn}(x) = \frac{d}{dx} |x|.$$

Then,  $\nabla_{\mathbf{x}} \mathbf{g}(\mathbf{x}^*) = \text{diag}\{\text{sgn}(x_1^*), \text{sgn}(x_2^*), \dots, \text{sgn}(x_n^*)\}$  is a diagonal matrix whose columns,  $(\partial g_j / \partial \mathbf{x})^T$  are linearly independent. The only pitfall is  $x_j^* = 0$ , where the sign function is indefinite. We assume that the optimal solutions  $x_j^*$  are nonzero because  $a_i \neq 0$ . This assumption will be relaxed later.


 Fig. 1. Graph of  $T(x)$ .

Now, substituting  $f(\mathbf{x})$ ,  $h(\mathbf{x})$  and  $\mathbf{g}(\mathbf{x})$  from (5)–(7) into (10)–(12), we obtain

$$2 \begin{bmatrix} x_1^* \\ x_2^* \\ \vdots \\ x_n^* \end{bmatrix} + \lambda \begin{bmatrix} a_1 \\ a_2 \\ \vdots \\ a_n \end{bmatrix} + \begin{bmatrix} \mu_1 \text{sgn}(x_1^*) \\ \mu_2 \text{sgn}(x_2^*) \\ \vdots \\ \mu_n \text{sgn}(x_n^*) \end{bmatrix} = \mathbf{0} \quad (13)$$

$$a_1 x_1^* + a_2 x_2^* + \cdots + a_n x_n^* - \tau_d = 0 \quad (14)$$

$$\mu_j (|x_j^*| - x_{\max}) = 0, \quad j \in \mathcal{J}. \quad (15)$$

Equations (13)–(15) constitute a set of  $2n + 1$  nonlinear equations with  $2n + 1$  unknowns  $\mathbf{x}^*$ ,  $\lambda$ , and  $\boldsymbol{\mu}$  to be solved in the following. Since  $\boldsymbol{\mu} \geq 0$  and  $\mathbf{g}(\mathbf{x}^*) \leq 0$ , (12) implies that  $\mu_i = 0$  for  $|x_j| < x_{\max}$ , and that  $\mu_j \geq 0$  for  $|x_j| = x_{\max}$ . Therefore, (13) can be written in the following compact form:

$$T(x_j^*) = -0.5\lambda a_j, \quad j \in \mathcal{J}. \quad (16)$$

The mapping  $T: \mathcal{D} \mapsto \mathfrak{R}$ , and  $\mathcal{D}(x) = \{x \in \mathfrak{R}: |x| \leq x_{\max}\}$ , is defined by

$$T(x) = \begin{cases} x, & |x| < x_{\max} \\ x + 0.5 \text{sgn}(x)\mu, & |x| = x_{\max} \end{cases} \quad (17)$$

where  $\mu_j$  is any positive number. The graph of the mapping is shown in Fig. 1. It is apparent from the figure that the mapping is invertible on  $\mathcal{D}$ , that is there exists a function  $T^{-1}(x)$  such that  $T^{-1}(T(x)) = x \forall x \in \mathcal{D}$ . In other words, the variable  $x_j^*$  in (16) can be determined uniquely if the right-hand-side of the equation is given. The inverse of the mapping is the saturation function, i.e.,  $T^{-1}(\cdot) \equiv \text{sat}(\cdot)$ , defined by

$$\text{sat}(x) = \begin{cases} x & |x| \leq x_{\max} \\ \text{sgn}(x)x_{\max} & \text{otherwise.} \end{cases} \quad (18)$$

Now, (16) can be rewritten as

$$x_j^* = \text{sat}(-0.5\lambda a_j), \quad j \in \mathcal{J}. \quad (19)$$

The above equation implies that  $x_j^* \neq 0$  as  $a_j \neq 0$ , which relaxes the assumption we made earlier. The second result is

that the larger the magnitude of the torque shape function  $|a_j|$ , the larger the magnitude of the optimal current  $x_j^*$ . If the phases are labeled in descending order

$$|a_1| \geq |a_2| \geq \cdots \geq |a_n| \implies |x_1^*| \geq |x_2^*| \geq \cdots \geq |x_n^*| \quad (20)$$

the optimal phase currents from  $x_1^*$  to  $x_n^*$  must be saturated consecutively. We use this fact to calculate the optimal phase currents consecutively in the same order, starting with  $x_1^*$ . In case saturation of a phase occurs, (19) implies that only knowing the sign of  $\lambda$  is enough to calculate the associate phase current. One can infer from (16) and (14) that

$$\text{sgn}(\tau_d) = \text{sgn}(-\lambda). \quad (21)$$

Therefore, if  $x_1^*$  saturates, then

$$x_1^* = \text{sgn}(-a_1\lambda)x_{\max} = \text{sgn}(a_1\tau_d)x_{\max}. \quad (22)$$

If  $x_1^*$  does not saturate, i.e.,  $|x_1^*| < x_{\max}$ , then neither does  $\{x_2, \dots, x_n\}$ , see (20). Let  $\lambda^{(1)}$  represents the Lagrangian multiplier when  $x_1^*$  does not saturate, then the Lagrangian multiplier can be calculated by substituting phase currents from  $x_j^* = -0.5\lambda a_j$  into (14)

$$\lambda^{(1)} = \frac{-2\tau_d}{\sum_{i=1}^n a_i^2} \quad (23)$$

which, in turn, can be substituted in (19) to obtain the optimal phase current

$$x_1^* = \text{sat} \left( \frac{a_1\tau_d}{\sum_{k=1}^n a_k^2} \right). \quad (24)$$

Since the denominator in (24) is always positive, by virtue of (22), one can infer that (22) provides the optimal solution for the saturation case as well. Analogously,  $x_2^*$  can be calculated if  $a_1 x_1^* - \tau_d$  is treated as the known parameter in (14). In general, the  $i$ th phase current can be calculated by induction as follows: since up to  $(i - 1)$ th phase currents have been already solved, we have

$$\underbrace{a_1 x_1^* + \cdots + a_{i-1} x_{i-1}^*}_{\text{known}} + \underbrace{a_i x_i^* + \cdots + a_n x_n^*}_{\text{unknown}} - \tau_d = 0. \quad (25)$$

The Lagrangian multiplier associated with the case of unsaturated  $x_i^*$  can be found from (19) and (25) as

$$\lambda^{(i)} = \frac{-2 \left( \tau_d - \sum_{k=1}^{i-1} a_k x_k^* \right)}{\sum_{k=i}^n a_k^2}. \quad (26)$$

Finally, substituting (26) in (19), gives the optimal phase currents, which produce the desired torque precisely, while mini-

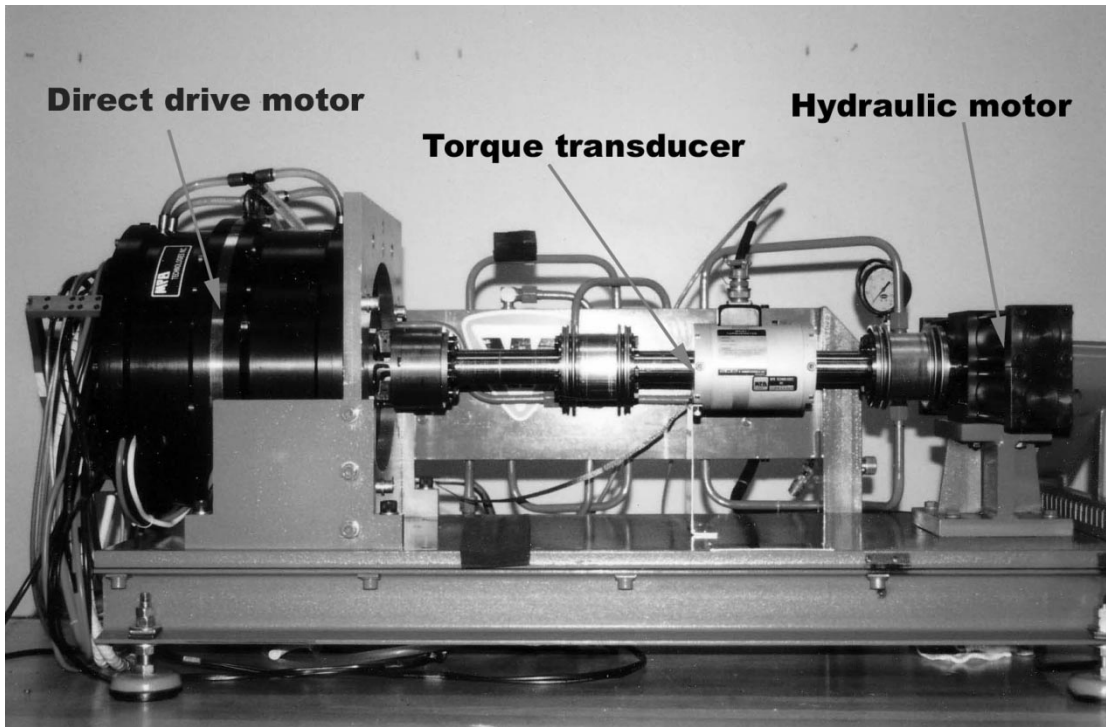


Fig. 2. Hydraulic dynamometer testbed.

mizing power losses, subject to the constraints of current saturation

$$x_i^* = \text{sat} \left( \frac{a_i \tau_d - a_i \sum_{k=1}^{i-1} a_k x_k^*}{\sum_{k=i}^n a_k^2} \right), \quad i = 2, \dots, n. \quad (27)$$

### III. MAXIMUM ATTAINABLE TORQUE

The control algorithm presented in Section II permits torque among phases when some phases saturate. How much torque is gained by this method? One can show [1] that the optimal solution of phase current without taking the saturation into account can be expressed explicitly in closed form as

$$x_j(\theta, \tau_d) = \frac{a_j \tau_d}{\sum_{k=1}^n a_k^2}, \quad \forall j \in \mathcal{J}. \quad (28)$$

In this case, the maximum torque depends on the saturation of the largest phase torque function. It is clear from (28) that, at any given motor position  $\theta$ , the phase with the largest torque shape function  $|a_j|$  reaches saturation first. Again, assuming that  $|a_1| \geq |a_2| \geq \dots \geq |a_n|$ , then maximum achievable torque can be calculated from (28)

$$\begin{aligned} |\tau_d| &\leq (|a_1| + |a_2/a_1||a_2| + \dots + |a_n/a_1||a_n|)x_{\max} \\ &= k_1(\theta)x_{\max}. \end{aligned} \quad (29)$$

On the other hand, the proposed algorithm increases the torque contribution of the unsaturated phases when one phase saturates,

until, in the limit, all phases are saturated. Hence, the maximum torque is

$$|\tau_d| \leq (|a_1| + |a_2| + \dots + |a_n|)x_{\max} = k_2(\theta)x_{\max}. \quad (30)$$

Both  $k_1(\theta) > 0$  and  $k_2(\theta) > 0$  are decisive factors in the torque capability of electric motors. Since  $|a_2/a_1| \leq 1, \dots, |a_n/a_1| \leq 1$ , one can conclude from (29) and (30) that  $k_1(\theta) \leq k_2(\theta)$ . The values of  $k_1$  and  $k_2$  depend on the torque shape functions,  $a_j$ . However, they can be expressed explicitly for an ideal three-phase motor, i.e.,  $n = 3$ , where we have a three shifted sinusoidal torque function as  $a_1(\theta) = \hat{a} \sin(\theta + \varphi)$ ,  $a_2(\theta) = \hat{a} \sin(\theta + 2\pi/3 + \varphi)$ , and  $a_3(\theta) = \hat{a} \sin(\theta + 4\pi/3 + \varphi)$ , where  $\varphi$  is an offset angle. In this case, using the properties of triangular functions, one can show that

$$\begin{aligned} 1.5\hat{a} &\leq k_1(\theta) \leq \sqrt{3}\hat{a} \\ \sqrt{3}\hat{a} &\leq k_2(\theta) \leq 2\hat{a}. \end{aligned}$$

Therefore, the maximum torque capability is boosted by  $2/\sqrt{3}$  (15.5%) when the phase saturation is considered in the phase current shape function.

### IV. EXPERIMENTAL PHASE TORQUE CHARACTERISTICS

#### A. Experimental Setup

Fig. 2 illustrates the experimental setup. The motor used for the testing is McGill/MIT synchronous motor [2], [7]. The motor and a hydraulic rack and pinion rotary motor are mounted on the rigid structure of the dynamometer. The hydraulic motor's shaft is connected to that of the direct-drive motor via a torque transducer (Himmelstein MCRT 2804TC) by means of two couplings which relieve bending moments or shear forces due to small axes misalignments. The speed of

the hydraulic motor is controlled by a pressure compensated flow control valve. The hydraulic pressure is set sufficiently high so that the hydraulic actuator regulates the angular speed regardless of the applied direct-drive motor torque. The motor torque is measured in a quasistatic condition, where the motor velocity is kept sufficiently low ( $1^\circ/\text{s}$ ), to ensure that the inertial torque does not interfere with the measurement. An adjustable cam and two limit switches detect the two rotational extremes and activate a solenoid valve through a PLC unit (not shown) to reverse the direction. The torque control system consists of three main functional components: position sensor, processor unit, and power amplifier. The position sensor is an optical encoder mounted to the motor shaft. Its mechanical resolution of 4500 lines per revolution is extended 80 times by an electronic interpolator for  $0.001^\circ$  resolution. The processor unit produces in real time the set points for the three phase current amplifiers. Three independent current servo amplifiers (Advanced Motion Control 30A20AC) control the motor's phase currents as specified by the processor. The amplifier's rated current and voltage are 15 A and 190 V with a switching rate of 22 kHz.

### B. Friction and Cogging Torques

In this section, we measure the torque shape functions by using the hydraulic dynamometer. To this end, the torque trajectory data versus position was logged during the rotation, while one phase was energized with a constant current. First, however, the joint friction and cogging torque are identified and then subtracted from the torque measurement. The cogging torque is attributed to residual magnetization in the stator armatures [16] or to presence of winding slots in the magnetic material, while the friction torque arises in the motor bearings and consists of viscous and dry friction. Since direct-drive motors operate at relatively low speeds, dry friction,  $\tau_F$ , dominates. The main practical problem in identifying the phase torque-angle characteristic is that the dry-friction is position dependent.

Let  $\tau_M(\theta)$  and  $\tau_F(\theta)$  represent the motor torque and the magnitude of the dry-friction. Then

$$\tau_M(\theta) = \tau(\theta) - \tau_F(\theta) \operatorname{sgn}(\dot{\theta}). \quad (31)$$

If  $\tau_M^+$  and  $\tau_M^-$  represent two sequences of motor torque measurements corresponding to clockwise and counter-clockwise rotations, then the magnetic and friction torques can be calculated as

$$\begin{aligned} \tau(\theta) &= \frac{1}{2} [\tau_M^+(\theta) + \tau_M^-(\theta)] \\ \tau_F(\theta) &= \frac{1}{2} [\tau_M^+(\theta) - \tau_M^-(\theta)]. \end{aligned} \quad (32)$$

The cogging torque can be measured by setting the phase current to zero. The dry friction, cogging, and the three phases' torque-angle profiles (with friction and cogging torques subtracted) are illustrated in Fig. 3 where the phase currents are individually set to 8 A. Although our experiments showed that friction torque with  $\pm 1$  Nm and cogging torques are relatively low, we compensate both for a more accurate torque generation.

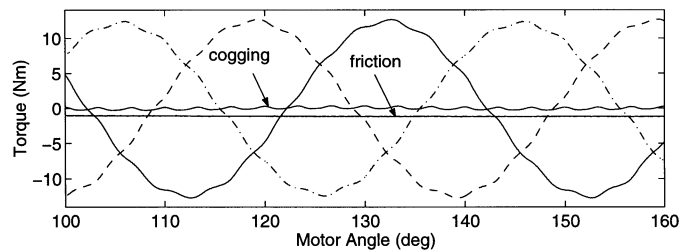


Fig. 3. Friction torque, cogging torque, and the three phase torque-angle profiles.

### C. Torque-Current Relationship

In this section, we investigate experimentally the torque-current relationship of our motor prototype. Graphical realization of torque-current over all positions is difficult due to the large number of plots required. This is greatly simplified in the frequency-domain because of the small numbers of harmonics. Since the motor has nine pole pairs, the torque trajectory is periodic in position with a fundamental spatial-frequency of nine cycles/revolution (cpr), and thus the torque pattern repeats every  $40^\circ$ , as shown in Fig. 3. The discrete Fourier series coefficients of the torque-position function is used to derive the spectrum. The frequency contents are expressed in harmonics of 9 cpr, i.e., the spatial frequency of the eleventh harmonics is 99 cpr. It turns out that the significant frequency components appear at the first, eleventh, and thirteenth harmonics.

Similar to the previous experiment, the torque-angle relationship is recorded within almost one rotation while the phase current is kept constant. But the current is incremented at the end of each rotation stroke by 1 A until an ensemble of torque profiles belonging to the span of  $[-15, 15]$  A is obtained. The major torque harmonics are plotted versus current in Fig. 4. It can be concluded from these experimental results that the torque is a linear function of current within the current range for this particular motor. However, we will still be able to demonstrate the capability of the proposed torque controller to compensate for phase current limitations—a similar limitation as saturation—in Section V.

## V. PERFORMANCE TEST

### A. Implementation of the Torque Control Algorithm

Assume that vector  $[a_j(\theta_1), a_j(\theta_2), \dots, a_j(\theta_p)] \in \mathbb{R}^p$  represents the discrete torque shape functions corresponding to  $p$  measurements of the phase torque (with unit current excitation) and positions. Then at any given position  $\theta$ , the corresponding shape function  $a_j(\theta)$  can be calculated via interpolation. The torque control algorithm is implemented as follows.

- 1) Interpolate the torque functions  $a_j$  for the current motor position.
- 2) Set  $x_j^* = 0$  for  $a_j = 0$  (or for sufficiently small  $|a_j|$ ).
- 3) Pick the set of nonzero shape functions and sort them such that  $|a_1| \geq |a_2| \geq \dots \geq |a_n|$  and calculate the optimal currents from equations (24) and (27). Go to step 1).

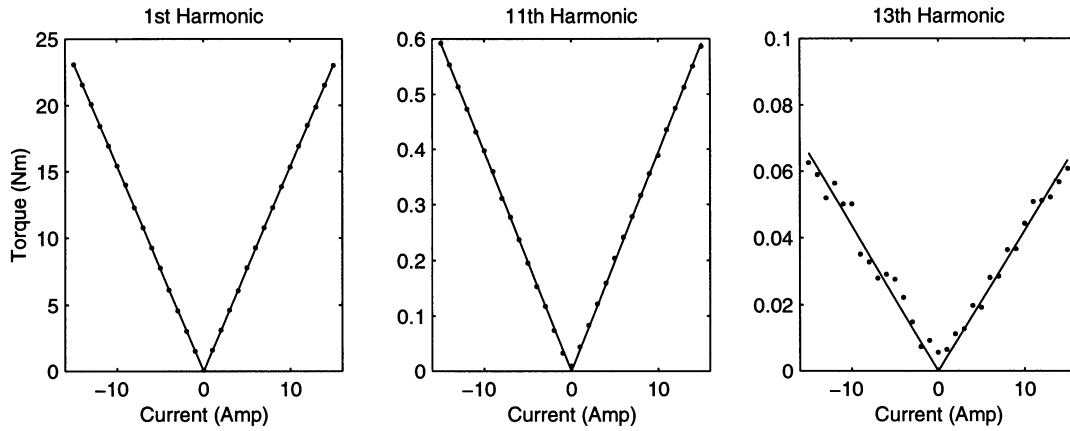


Fig. 4. Magnitude of torque harmonics versus phase current.

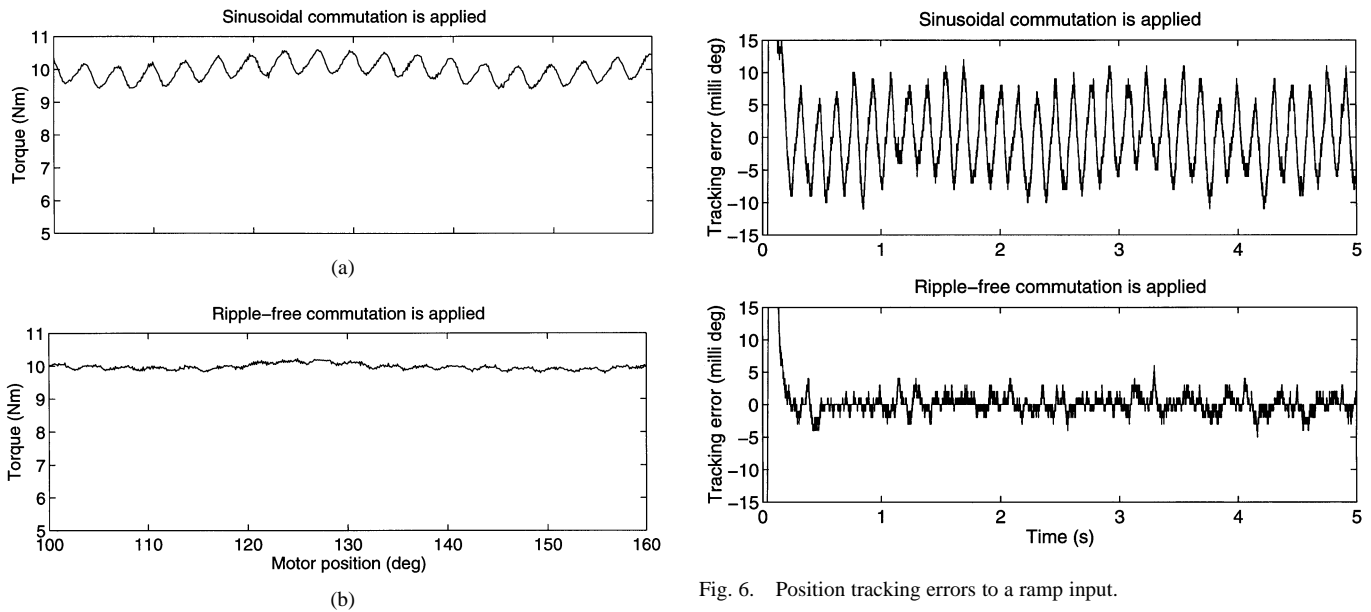


Fig. 5. Motor torque in (a) sinusoidal and (b) ripple free commutations.

### B. Torque Ripple

The torque controller was tested on the dynamometer. Again, the motor shaft is rotated by the hydraulic actuator while the motor torque is monitored by the torque transducer. Fig. 5 shows the motor torque versus position when standard sinusoidal commutation and our torque controller are applied. Clearly, a drastic reduction in torque ripple is achieved.

### C. Effect of Torque Ripple in Motion Control

A motor's torque ripple acts as a perturbation to the control system, degrading the tracking performance, especially at low velocities. We examine the position tracking accuracy of our direct-drive system with and without torque ripple. To this end, a proportional integral derivative (PID) position controller  $\tau_d = K_P e + K_I \int e dt + K_D \dot{e}$ , where  $e = \theta_d - \theta$ , (Gains:  $K_P = 30 \text{ Nm}^\circ$ ,  $K_I = 200 \text{ Nm}^\circ/\text{s}$ ,  $K_D = 0.65 \text{ Nm}^\circ/\text{s}^\circ$ ) is implemented, in addition to the torque controller. Fig. 6 documents the tracking error of the system to a ramp input, that is equivalent

Fig. 6. Position tracking errors to a ramp input.

to a step input velocity of  $20^\circ/\text{s}$ , when (a) the sinusoidal commutation and (b) our controller are applied. The figure clearly shows that the tracking error is limited by the torque ripple. In the absence of actuator torque ripples, the tracking error is reduced down to about the encoder resolution ( $0.001^\circ$ ).

### D. Torque Saturation

By how much does the proposed controller improve the maximum torque capability of our motor prototype? This is investigated by comparing the maximum torque produced by the motor prototype when our proposed torque controller (27) and the conventional one (28) are applied. Fig. 7 shows the graphs of the maximum achievable torque with respect to maximum phase current  $x_{\max} = 15 \text{ A}$ . The solid line and the dashed line depicted the maximum attainable torque with respect to the proposed controller (27) and conventional controller (28), respectively. As described in Section III the torque saturation points differs from one position to another. Therefore, only the lowest torque value is available over all motor positions without having saturation induced torque ripple. It is evident from the graphs that the motor torque limits corresponding to the optimal torque

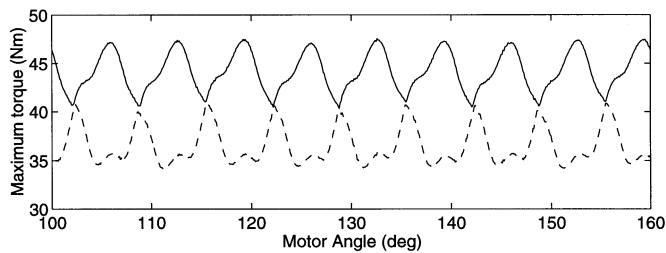


Fig. 7. Maximum admissible torque corresponding to maximum phase current 15 A. Solid: with torque sharing and dashed: without torque sharing.

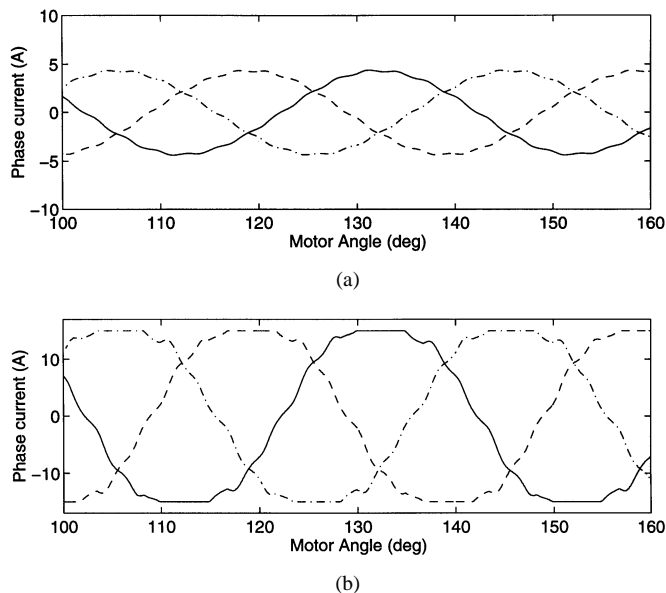


Fig. 8. Phase current with the requested torque (top) 10 Nm and (bottom) 38 Nm, respectively.

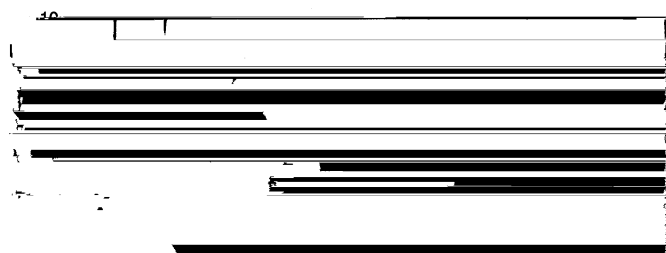


Fig. 9. Phase current profile when the motor operate only with two phases.

controllers (27) and (28), i.e., with and without taking current saturation into account, are 34 Nm and 41 Nm—an increase of 20%!

One aspect of our proposed torque control algorithm is the current-position pattern varies with requested torque. This is demonstrated in Fig. 8 (a) and (b) which show the current-position pattern of the motor with respect to the requested torques 10 Nm and 38 Nm, respectively.

### E. Two-Phase Commutation

One interesting aspect of the proposed controller is that it does not rely on any condition on the torque-position pattern of the phases, such as having balanced phases, where  $\sum a_j = 0$  [6]. Therefore, the control algorithm can achieve ripple-free

torque even if a motor phase fails. As an illustration, Fig. 9 shows the phase currents of two phases producing the same torque 10 Nm as the three phases in Fig. 8 (a). This can be useful in practice when there is a need to continue operating the motor even in the case of a phase failure. However, the price is a higher power consumption—in this particular case from 75 W to 128 W.

## VI. CONCLUSION

The motor torque control problem was viewed as the optimization of a nonlinear mapping from commanded torque and motor position to commanded phase currents. We have formulated the problem with copper losses as the cost function while the torque equation and current saturation enter as equality and inequality constraints. The optimal phase current minimizing the copper losses subject to the ripple-free torque constraint and the phase current saturation constraint has been solved via the Kuhn–Tucker theorem. The solution is explicitly presented as a mapping of the current phases versus torque setpoints and motor angular position. We showed that by considering current saturation in design, the optimal current–angle waveform varies to compensate for phase current saturation so that maximum torque capability of motor is increased.

A hydraulic dynamometer has been used to characterize the torque–angle and torque–current characteristics of our direct-drive motor’s phases. The proposed torque control algorithm has been implemented in real-time. Experimental results have shown that torque-ripple is almost eliminated and, as a result, position tracking error was reduced dramatically to about the encoder resolution. We also showed that by considering current saturation in the design of torque control, the maximum torque capability of our motor was increased by 20% compared with fixed current–angle commutation.

## REFERENCES

- [1] F. Aghili, M. Buehler, and J. M. Hollerbach, “Torque ripple minimization in direct-drive systems,” in *Proc. IEEE/RSJ Int. Conf. Intelligent Systems and Robots*, Victoria, BC, Canada, Oct. 1998, pp. 794–799.
- [2] —, “Development of a high performance direct-drive joint,” *Adv. Robotics*, vol. 16, no. 3, pp. 233–250, Oct. 2002.
- [3] —, “Optimal commutation laws in the frequency domain for pm synchronous direct-drive motors,” *IEEE Trans. Power Electron.*, vol. 15, pp. 1056–1064, Nov. 2000.
- [4] E. Favre, L. Cardoletti, and M. Jufer, “Permanent-magnet synchronous motors: A comprehensive approach to cogging torque suppression,” *IEEE Trans. Ind. Applicat.*, vol. 29, pp. 1141–1149, Nov. 1993.
- [5] F. Filicori, C. G. Lo Bianco, and A. Tonielli, “Modeling and control strategies for a variable reluctance direct-drive motor,” *IEEE Trans. Ind. Electron.*, vol. 40, pp. 105–115, Feb. 1993.
- [6] I. Ha and C. Kang, “Explicit characterization of all feedback linearizing controllers for a general type of brushless dc motor,” *IEEE Trans. Automat. Contr.*, vol. 39, pp. 673–677, Mar. 1994.
- [7] J. M. Hollerbach, I. Hunter, J. Lang, S. Umans, and R. Sepe, “The McGill/MIT Direct Drive Motor Project,” in *Proc. IEEE Int. Conf. Robotics Automation*, May 1993, pp. 611–617.
- [8] Y. Y. Hung and Z. Ding, “Design of currents to reduce torque ripple in brushless permanent magnet motors,” *Proc. Inst. Elect. Eng.*, vol. 140, no. 4, 1993.
- [9] M. Ilic’-Spong, R. Marino, S. M. Peresada, and D. G. Taylor, “Feedback linearizing control of switched reluctance motors,” *IEEE Trans. Automat. Contr.*, vol. AC-32, pp. 371–379, May 1987.
- [10] H. W. Kuhn and A. W. Tucker, “Nonlinear programming,” in *Proc. 2nd Berkeley Symposium Mathematical Statistics Probability*. Berkeley, CA: Univ. California Press, 1951, pp. 481–492.

- [11] H. Le-Huy, R. Perret, and R. Feuillet, "Minimization of torque ripple in brushless dc motor drives," *IEEE Trans. Ind. Applicat.*, vol. IA-22, pp. 748–755, Sept. 1986.
- [12] D. G. Manzer, M. Varghese, and J. S. Thorp, "Variable reluctance motor characterization," *IEEE Trans. Ind. Electron.*, vol. 36, pp. 56–63, Feb. 1989.
- [13] Y. Murai, Y. Kawase, K. Ohashi, and K. Okuyama, "Torque ripple improvement for brushless dc miniature motors," *IEEE Trans. Ind. Applicat.*, vol. 25, pp. 441–449, May 1993.
- [14] K. R. Shouse and D. G. Taylor, "A digital self-tuning tracking controller for pm synchronous motors," in *IEEE Conf. Decision Control*, San Antonio, TX, 1992, pp. 3397–3402.
- [15] —, "Observer based control of pm synchronous motors," in *Int. Conf. Industrial Electronics, Control, Instrumentation and Automation*, San Diego, CA, 1992, pp. 1482–1487.
- [16] D. G. Taylor, "Nonlinear control of electric machines: An overview," *IEEE Contr. Syst. Mag.*, vol. 14, pp. 41–51, 1994.
- [17] —, "Digital reduced-order modeling and feedback for nonlinear systems," in *Proc. Workshop Advances Control Applications*. New York, 1996, pp. 257–281.
- [18] D. G. Taylor, M. Ilic'-Spong, R. Marino, and S. Peresada, "A feedback linearizing control for direct-drive robots with switched reluctance motors," in *Proc. IEEE Int. Conf. Decision Contr.*, Miami Beach, FL, Dec. 1986, pp. 388–396.
- [19] R. S. Wallace and D. G. Taylor, "Low-torque-ripple switched reluctance motors for direct-drive robotics," *IEEE Trans. Robot. Automat.*, vol. 7, pp. 733–742, Dec. 1991.